https://doi.org/10.5194/egusphere-2026-3201
Preprint. Discussion started: 1 September 2026
© Author(s) 2026. CC BY 4.0 License.

Effects of atmospheric turbulence on vertical dispersion of carbon dioxide and methane over subtropical paddy fields

Jiawei Yan[1], Lu Zhang[1,*], Yizhou Xu[1], Xinfeng Ling[2], Weiwei Ding[2], Yubin Li[1], Yuan Wang[1], Yuanjian Yang[1]

[1]School of Atmospheric Physics, Nanjing University of Information Science & Technology, Nanjing, China
[2]Shouxian National Climatology Observatory, Huainan, China

Correspondence to: Lu Zhang (luzhang@nuist.edu.cn)

Abstract. Paddy fields serve as a critical methane (CH_4) source and carbon dioxide (CO_2) sink, playing an essential role in terrestrial carbon cycling and greenhouse gas budgets. The effects of atmospheric turbulence on the vertical dispersion of CO_2 and CH_4 were investigated in this study, using high-frequency observations over subtropical paddy fields. The pronounced diurnal variations in surface concentrations and turbulent fluxes of both gases suggest the dominant control of boundary-layer turbulent diffusion. Focusing on nocturnal stable conditions, mutual information was introduced to characterize relevant nonlinear processes. Turbulence over the paddy fields becomes intermittent when the nighttime wind speed falls below 1.5 m s^{-1}. This weak and intermittent turbulence generally leads to the accumulation of CO_2 and CH_4 near the surface, whereas short turbulent bursts promote rapid dispersion, showing strong non-stationarity. Under intermittent turbulence, interference from submeso motions renders similarity relationships inapplicable for describing the transport of momentum, heat, as well as passive scalars (CO_2 and CH_4). This limitation can be effectively mitigated by removing submeso components from original observations. The distinct spectral gap between submeso and turbulent scales indicates the breakdown of energy cascade. As submeso energy is confined to its original scale, the energy supply for small-scale turbulence is limited and turbulence becomes more stochastic. This study reveals the effects of intermittent turbulence on the vertical diffusion of CO_2 and CH_4 under nocturnal stable conditions, but also highlights the challenges in parameterizing such stable-boundary-layer processes. This provides new insights for understanding carbon cycling over terrestrial ecosystems.

1 Introduction

As typical constructed wetland ecosystems, paddy fields play a critical role in terrestrial carbon cycling and greenhouse gas budgets. They act as an important carbon sink by sequestering atmospheric CO_2 through photosynthesis during the day, while releasing CO_2 through ecosystem respiration at night. Meanwhile, paddy fields also act as a dominant source of atmospheric methane (CH_4), accounting for over 37 % of agricultural CH_4 emissions (IPCC, 2021; MEE, 2024). Therefore, an in-depth insight into the vertical dispersion dynamics of CO_2 and CH_4 over paddy fields is essential for reliably assessing terrestrial carbon cycles and their climatic implications.

https://doi.org/10.5194/egusphere-2026-3201
Preprint. Discussion started: 1 September 2026
© Author(s) 2026. CC BY 4.0 License.

Atmospheric turbulence governs the vertical exchange of momentum, heat, and substances (e.g., CO_2 and CH_4) between the land surface and the atmosphere (Stull, 1988; Foken, 2008; Tang et al., 2016). The Monin–Obukhov similarity theory (MOST) was established to describe the turbulent transport processes of various physical quantities under ideal conditions (Monin and Obukhov, 1954), and has been widely adopted in numerical atmospheric models (Businger et al., 1971; Jiménez et al., 2012; Jason et al., 2023; Tamanna et al., 2026). However, under very weak wind and stable conditions, turbulence becomes weak, spatially discontinuous, and temporally non-stationary, which is referred to as intermittent turbulence (e.g., Mahrt, 2014; Yus-Díez et al., 2019; Zhang, 2024). In such regimes, MOST is no longer applicable (Acevedo et al., 2014), which accounts for the poor modelling performance in the stable nocturnal boundary layer (Nappo et al., 2014; Wang et al., 2015; Mohammad et al., 2024). Furthermore, intermittent turbulence is widely acknowledged to modulate land–atmosphere exchange within the very stable boundary layer. Typical examples include the continuous accumulation and rapid dissipation of anthropogenic pollutants near the surface (Wei et al., 2018; Ren et al., 2021), the downward dispersion of long-range transported dust aerosols (Zhang, 2022), and the vertical mixing of ozone from the residual layer down toward the surface (Salmond, 2005). Over subtropical paddy fields, intermittent turbulence is also non-negligible (Zhang et al., 2026). Nevertheless, the mechanisms by which intermittent turbulence regulates the vertical dispersion of the key greenhouse gases CO_2 and CH_4 remain poorly understood, thereby motivating this study.

Turbulent flow is inherently a stochastic and nonlinear system, particularly in the case of intermittent turbulence. Thus, accurately characterizing intermittent turbulence remains a challenge (Mahrt, 2014). Information theory provides an alternative framework for describing the physical features of complex systems (Shannon, 1948, 1949; McGill, 1954), as it does not rely on linear assumptions. It has been widely applied in laboratory turbulence research (e.g., Ikeda, 1989). The Kullback–Leibler (KL) divergence has been employed to identify the laminar–turbulent transition in pipe flow and non-Gaussian characteristics within turbulent boundary layers (Tsuji and Nakamura, 1999; Raj et al., 2025). Shavit and Falkovich (2020) pointed out that mutual information reflects physical correlations between variables in a given complex system (e.g., turbulent field), and they adopted mutual information to quantify information flow between different scales in weak turbulence. On this basis, Bahamonde et al. (2023) revealed that a decline in mutual information is generally accompanied by the Gaussianization of corresponding variables' probability distribution. The reliability of the information theory-based method has been well validated in laboratory flow experiments, which offers a potential new approach for characterizing intermittent turbulence in the atmospheric boundary layer.

Therefore, this study aims to investigate the effects of intermittent turbulence on the vertical dispersion of two major greenhouse gases, CO_2 and CH_4, using high-frequency observations over subtropical paddy fields. The novelty lies in the introduction of mutual information to quantify the nonlinear relationships among turbulent intermittency, meteorological conditions, and gas concentrations. This study is organized as follows: Section 2 describes the experimental site and data processing, followed by a brief introduction of methods in Section 3; Section 4 presents the results and discusses them. Section 5 presents the conclusions of this study.

https://doi.org/10.5194/egusphere-2026-3201
Preprint. Discussion started: 1 September 2026
© Author(s) 2026. CC BY 4.0 License.

2 Description of the site and data

2.1 Experimental site

The observational data used in this study were collected at the Shouxian National Climatological Observatory (32.44° N, 116.79° E) from 1 to 31 August 2024. The site is located in a prime farmland area in the middle reaches of the Huaihe River Basin and is surrounded by extensive, homogeneous paddy fields throughout the observational period. An eddy covariance system was installed at a height of 4 m on a 32 m meteorological tower. The system comprises a three-dimensional sonic anemometer (CSAT3A, Campbell Scientific Inc., USA), an open-path CO_2/H_2O gas analyzer (EC150, Campbell Scientific Inc., USA), and an open-path CH_4 gas analyzer (LI-7700, LI-COR Inc., USA). It measured three-dimensional wind components, air temperature, and mass concentrations of water vapor, CO_2, and CH_4 at a frequency of 10 Hz. Mean meteorological variables, including air temperature, humidity, and wind vector, were measured at heights of 2, 4, 10, 20, and 30 m on the tower. In addition, radiation components were monitored by a four-component net radiometer (CNR4, Kipp & Zonen, Netherlands). For comparison with local CO_2 and CH_4 variations, $PM_{2.5}$ concentrations obtained from a particulate matter monitor (GRIMM EDM 180, Durag Group, Germany) were also considered in this study. The variations of $PM_{2.5}$ concentrations mainly reflect the influence of advection, since anthropogenic emissions in the vicinity of the observation site are nearly negligible.

During the observation period, rice transitioned from the reproductive stage (early to mid-August) to the ripening stage (late August). At the reproductive stage, the rice plant height reached approximately 0.9 m with dense foliage, leading daytime CO_2 flux to its annual peak (Duan et al., 2022). Meanwhile, continuous irrigation maintained a ponded water layer of about 0.05 m on the soil surface. The oxygen-depleted soil environment substantially enhanced CH_4 emissions. The combination of these factors provides ideal conditions for investigating the vertical dispersion of CO_2 and CH_4. At the ripening stage, rice leaves gradually withered, and field irrigation was discontinued. As the soil surface dried out, CH_4 emissions decreased correspondingly.

2.2 Data processing

The raw high-frequency data observed from the eddy covariance system were processed over 30 min intervals using EddyPro software (Advanced v7.0.6, LI-COR Inc., USA). The processing procedure mainly involved error flags, despiking (Vickers and Mahrt, 1997), double coordinate rotations, Reynolds decomposition, and linear detrending, to obtain Reynolds means and fluctuations. Furthermore, the density correction (Webb et al., 1980) is applied to the fluctuations of water vapor, CO_2, and CH_4 concentrations, following Detto et al. (2008). Then, turbulent statistics, including sensible heat flux (H), latent heat flux (LE), CO_2 flux (F_{CO_2}), CH_4 flux (F_{CH_4}), momentum flux (τ), turbulent kinetic energy (TKE), friction velocity (u_*), temperature scale (θ_*), specific humidity scale (q_*), CO_2 concentration scale (CO_{2*}), and CH_4 concentration scale (CH_{4*}) are calculated using the eddy covariance method:

$$H = \rho_a c_p \overline{w'\theta'}, \quad (1)$$

https://doi.org/10.5194/egusphere-2026-3201
Preprint. Discussion started: 1 September 2026
© Author(s) 2026. CC BY 4.0 License.

$$LE = \rho_a L_v \overline{w'q'}, \quad (2)$$

$$F_{CO_2} = \overline{w'\rho'_{CO_2}}, \quad (3)$$

$$F_{CH_4} = \overline{w'\rho'_{CH_4}}, \quad (4)$$

$$\tau = -\rho_a \left(\overline{u'w'}^2 + \overline{v'w'}^2\right)^{1/2}, \quad (5)$$

$$\mathrm{TKE} = \frac{1}{2}\left(\overline{u'^2} + \overline{v'^2} + \overline{w'^2}\right), \quad (6)$$

$$u_* = \left[\left(-\overline{u'w'}\right)^2 + \left(-\overline{v'w'}\right)^2\right]^{1/4}, \quad (7)$$

$$a_* = -\overline{w'a'}/u_*, a = \theta, q, CO_2, CH_4, \quad (8)$$

where u, v, and w are along-wind, across-wind and vertical velocity components, respectively; θ, q, ρ_{CO_2}, and ρ_{CH_4} are potential temperature, specific humidity, CO_2 molar density, and CH_4 molar density, respectively; ρ_a, c_p, and L_v are air density, specific heat capacity at constant pressure, and specific evaporation heat, respectively. The prime and overbar denote the turbulent fluctuations and Reynolds means, respectively. The local Obukhov length is calculated as

$$L = -\bar{\theta}u_*^3/\kappa g\overline{w'\theta'}, \quad (9)$$

where κ is the von Kármán constant (0.4) and g is the gravitational acceleration (9.81 m s^{-2}). The atmospheric stability parameter is represented by $\zeta = z/L$ where z is the measurement height. Additionally, the bulk Richardson number is also used to represent atmospheric stability from the perspective of mean meteorological field. It is calculated as follows:

$$R_B = \frac{g}{\bar{\theta}}\left(\frac{\bar{\theta}_2 - \bar{\theta}_1}{z_2 - z_1}\right) / \left(\frac{\bar{u}_2 - \bar{u}_1}{z_2 - z_1}\right)^2, \quad (10)$$

where $\bar{\theta}_1$ ($\bar{u}_1$) and $\bar{\theta}_2$ ($\bar{u}_2$) are the mean potential temperature (wind speed) at the height of z_1 (i.e., 4 m) and z_2 (i.e., 10 m), respectively, and $\bar{\theta}$ is the mean potential temperature at 4 m.

Specifically, quality controls on the turbulence data were performed in Sect. 4.3. Only the 30 min data records satisfying the following criteria were selected for analysis: (a) The atmospheric stability parameter ζ should be less than zero in the daytime and greater than zero in the nighttime; (b) For observations of continuous turbulence, friction velocity u_* should be greater than 0.02 m s^{-1}. Meanwhile, the absolute values of CO_2 flux, CH_4 flux should be greater than 8 μmol m^{-2} s^{-1}, 0.5 μmol m^{-2} s^{-1}, respectively, to ensure that turbulent fluxes can be well resolved.

3 Method

3.1 Hilbert–Huang Transform

The Hilbert–Huang Transform (HHT) is fully data driven, adaptive without prior assumptions, and local in both physical and frequency domain (Huang et al., 2008). Its reliability in processing nonlinear and nonstationary signals, such as intermittent

https://doi.org/10.5194/egusphere-2026-3201
Preprint. Discussion started: 1 September 2026
© Author(s) 2026. CC BY 4.0 License.

turbulence, has been demonstrated by Wei et al. (2016, 2017). In this study, this technique was adopted to decompose the time series of fluctuations (i.e., u', v', w', and θ') into turbulent and submeso parts, and then to quantify the intermittent intensity. To perform the HHT, 30 min fluctuations (u', v', w' or θ') are first decomposed into a set of intrinsic mode functions (IMFs) with different mean frequencies using the empirical mode decomposition (EMD). The decomposition can be expressed as follows:

$$X(t) = \sum_{n=1}^{k} c_n(t) + r_k(t), \tag{11}$$

where $X(t)$ denotes the time series of fluctuations; $c_n(t)$ and $r_k(t)$ represent the n-th IMF component and residual term, respectively; and k is the total number of IMFs. Then, the second-order Hilbert spectra $L_2(\omega)$, which correspond to the distribution of energy, are calculated by the marginal integration of joint probability density function $p(\omega, A)$ (Huang et al., 2008; Wei et al., 2016):

$$L_2(\omega) = \int p(\omega, A) A^2 \mathrm{d}A, \tag{12}$$

where ω denotes the instantaneous frequency and A is the instantaneous amplitude. According to Zhang et al. (2024), the critical frequency is defined as the frequency satisfying the following criteria: (a) Beyond which the spectral slope begins to significantly deviate from the Kaimal et al. (1972) spectra model (with a threshold of 0.5 adopted); and (b) the peak value on the low-frequency side is significantly greater than that of high-frequency side (for which a threshold of 5 was adopted). Based on the critical frequency, the original fluctuating time series can be decomposed into turbulent and submeso parts as follows:

$$X(t) = \sum_{n=1}^{k_0} c_n(t) + \sum_{n=k_0+1}^{k} c_n(t), \tag{13}$$

where k_0 is the order of the critical mode whose mean frequency is closest to the critical frequency; $\sum_{n=1}^{k_0} c_n(t)$ ($\sum_{n=k_0+1}^{k} c_n(t)$) represents the sum of IMFs whose mean frequency is higher than (lower than) the critical frequency, corresponding to the turbulent (submeso) part.

Applying the above HHT-based decomposition to three-dimensional velocity components, yields the turbulent velocities (u'_{turb}, v'_{turb}, and w'_{turb}) and submeso velocities (u'_{smeso}, v'_{smeso}, and w'_{smeso}). The velocity scales of turbulent and submeso motions are thereby denoted as (Mahrt, 2009):

$$V_{\mathrm{smeso}} = \sqrt{\overline{u'^2_{\mathrm{smeso}}} + \overline{v'^2_{\mathrm{smeso}}} + \overline{w'^2_{\mathrm{smeso}}}}, \tag{14}$$

$$V_{\mathrm{turb}} = \sqrt{\overline{u'^2_{\mathrm{turb}}} + \overline{v'^2_{\mathrm{turb}}} + \overline{w'^2_{\mathrm{turb}}}}, \tag{15}$$

where the subscripts turb and smeso represent the turbulent and submeso parts, respectively. Finally, the local intermittent strength of turbulence (LIST; Ren et al., 2019) is calculated by:

$$\mathrm{LIST} = \frac{V_{\mathrm{turb}}}{\sqrt{V^2_{\mathrm{turb}} + V^2_{\mathrm{smeso}}}}, \tag{16}$$

which can be understood as the ratio of turbulent velocity scale to total velocity scale. When LIST approaches one, the influence of submeso motions is weak, and turbulence is continuous. Conversely, a small value of LIST suggests that

https://doi.org/10.5194/egusphere-2026-3201
Preprint. Discussion started: 1 September 2026
© Author(s) 2026. CC BY 4.0 License.

turbulence is suppressed by submeso motions and displays intermittency. Following Zhang et al. (2024), a threshold of 0.75 was adopted to distinguish between intermittent turbulence and continuous turbulence in this study.

3.2 Fourier spectral analysis

Using the Fourier transform technique, the time series of a given variable $X(t)$ is mapped to the frequency domain to derive its power spectral density distribution:

$$S_a(f) = \sigma_a^2 \int_{-\infty}^{+\infty} X(t) e^{-i2\pi f t} \mathrm{d}t, \quad (17)$$

where f is the natural frequency, $S_a(f)$ is the power spectral density, and σ_a^2 is the variance of the given variable. In this study, Fourier spectral analysis is applied to the one-month time series of CO_2, CH_4, and $PM_{2.5}$ concentrations at a 30 min resolution, as well as to the 30 min time series of fluctuations at a 10 Hz resolution. For the former, the dominant scale (and corresponding atmospheric physical processes) of each substance concentration can be identified from the peaks of the power spectra. For the latter, the turbulence energy spectra are derived, which reveal the microscale characteristics of turbulent structures and the modulation induced by submeso motions.

3.3 Mutual information

In information theory, information entropy is a measure of the uncertainty of a random variable, representing the average amount of information required to characterize its statistical properties (Shannon, 1948; McGill, 1954). For a random variable X, information entropy is defined as:

$$H(X) = -\int \rho(x) \log \rho(x) \mathrm{d}x, \quad (18)$$

where $\rho(x)$ is the probability density function of the variable X. For a pair of random variables (X, Y), their joint information entropy is expressed as:

$$H(X,Y) = -\iint \rho(x,y) \log \rho(x,y) \, \mathrm{d}x \, \mathrm{d}y, \quad (19)$$

where $\rho(x,y)$ is the joint probability density function of (X,Y). $H(X,Y)$ measures the average amount of information required to describe the system (X,Y). If the two variables are physically correlated, the sum of their individual entropies is always greater than the entropy of the coupled system. The difference between the theoretical maximum information amount of the system and its actual information amount $(H(X) + H(Y) - H(X,Y))$, represents the information transmitted and shared between the two variables; this is known as mutual information $I(X;Y)$. Similar to information entropy, mutual information is also calculated as:

$$I(X;Y) = \iint \rho(x,y) \log \frac{\rho(x,y)}{\rho(x)\rho(y)} \mathrm{d}x \, \mathrm{d}y, \quad (20)$$

From a physical perspective, mutual information reflects the intrinsic nonlinear correlation and mutual constraint between two variables (Cover and Thomas, 2006; Bahamonde et al., 2023). Compared with conventional linear correlation metrics, its advantage lies in requiring no prior assumptions regarding the data distribution. Mutual information between variables can be normalized by information entropy as follows:

https://doi.org/10.5194/egusphere-2026-3201
Preprint. Discussion started: 1 September 2026
© Author(s) 2026. CC BY 4.0 License.

$$I_N = \frac{I(X;Y)}{\sqrt{(H(X)H(Y))}}. \quad (21)$$

Furthermore, mutual information is used to quantify the amount of information transmitted from the current turbulent fluctuation (i.e., $u(t)$) to its increment $\delta u = u(t+\tau) - u(t)$, thereby characterizing the memory and evolution of turbulent field over a time interval τ:

$$I(u; \triangle u) = \iint \rho(u, \delta u) \log \frac{\rho(u,\delta u)}{\rho(u)\rho(\delta u)} \mathrm{d}u \, \mathrm{d}\delta u, \quad (22)$$

The magnitude of mutual information represents the strength of the nonlinear constraint between the current state and the future state of the turbulent field. A larger value indicates that the turbulent field retains more correlation and information over time, while a smaller value implies rapid dissipation of temporal correlation and enhanced randomness of the turbulent field. Furthermore, to compare mutual information at different scales, the time lag τ is normalized by integral time scale τ_0 as follows:

$$\tau_0 = \int_0^\infty r(\xi) \, \mathrm{d}\xi, \quad (23)$$

where ξ is the time lag, and $r(\xi)$ is the autocorrelation coefficient of the turbulent fluctuations with a time lag ξ. The integral time scale τ_0 represents the average lifetime of turbulent eddies.

4 Results and discussion

4.1 Meteorological background and characteristics of substance concentrations

Figure 1 presents the time series of meteorological variables and the concentrations of CO_2, CH_4, and $PM_{2.5}$ over Shouxian rice paddy in August 2024. The observation period was divided into three stages according to the temporal variations in CO_2, CH_4, and $PM_{2.5}$ concentrations. From 1 to 7 August (Stage 1), all three tracers exhibited similar diurnal variations, with higher concentrations at night and lower values in the daytime. In particular, the variations of CO_2 and CH_4 concentrations were highly consistent (Fig. 1e), with a correlation coefficient of 0.93. From 8 to 19 August (Stage 2), the CO_2 and CH_4 concentrations still maintained the diurnal pattern of nocturnal maxima and daytime minima, though their amplitudes gradually weakened. In contrast, the diurnal pattern of $PM_{2.5}$ concentration reversed, with lower concentrations at night and higher during the daytime; its concentration peak occurred in the morning. Finally, from 20 to 31 August (Stage 3), asynchronous variations among the concentrations of the three tracers became more pronounced. The CO_2 concentration substantially increased (exceeding 450 ppm), accompanied by considerable day-to-day variability. Meanwhile, CH_4 concentration decreased markedly and exhibited weak diurnal variation. $PM_{2.5}$ concentration exhibited a periodic variation of 4–5 days with a ramp-like structure, which suggests a possible influence of synoptic-scale processes.

https://doi.org/10.5194/egusphere-2026-3201
Preprint. Discussion started: 1 September 2026
© Author(s) 2026. CC BY 4.0 License.

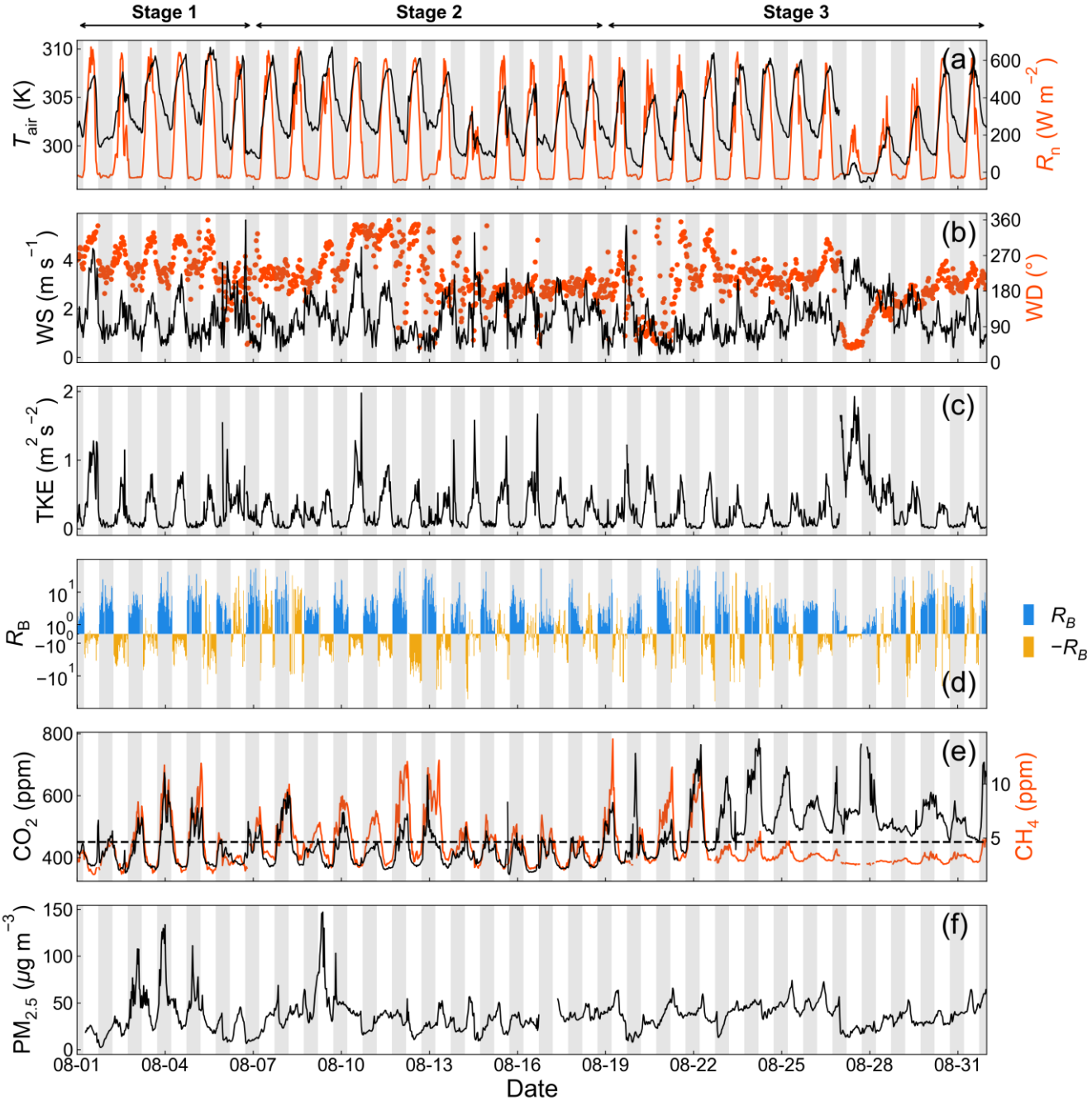

Figure 1. Time series of meteorological variables and substance concentrations at the Shouxian rice paddy site in August 2024. (a) air temperature (black line) and net radiation (red line), (b) wind speed (black line) and wind direction (red circles), (c) turbulent kinetic energy, (d) bulk Richardson number, (e) CO_2 (black line) and CH_4 (red line) concentrations, and (f) $PM_{2.5}$ mass concentration. In panel (d), the blue and yellow bars represent positive and negative values, respectively. In panel (e), dashed lines denote the thresholds of CO_2 concentration of 450 ppm. The shaded areas represent nighttime.

https://doi.org/10.5194/egusphere-2026-3201
Preprint. Discussion started: 1 September 2026
© Author(s) 2026. CC BY 4.0 License.

During Stage 1, the concentrations of CO_2, CH_4, and $PM_{2.5}$ were mainly regulated by the development of atmospheric boundary layer and its internal turbulent activities. After sunrise, as the surface temperature rose, positive buoyancy efficiently generated turbulence and promotes boundary-layer growth. These processes provided both dynamic driving and sufficient space for the vertical dispersion of the three tracers, leading to a notable decrease in near-surface concentrations (Figs. 1e–f). Conversely, as land surface radiatively cooled after sunset, negative buoyancy began to dissipate TKE. Combined with light wind conditions, for example the nighttime of 3–4 August (Fig. 1b), the shear production of TKE was possibly insufficient to balance the consumption by negative buoyancy (Zhang et al., 2026). As a result, turbulence nearly decayed (Fig. 1c), and the vertical exchange was greatly suppressed (Mahrt, 2014). Consequently, locally emitted CO_2 and CH_4, as well as $PM_{2.5}$, accumulated within the surface layer, with peak values exceeding 600 ppm, 10 ppm, and 100 μg m^{-3}, respectively. In Stage 2, nocturnal wind speed generally increased (Fig. 1b), particularly during 13–18 August, with values above 1.5 m s^{-1}. Stronger nocturnal winds sustained turbulent motions, suggested by the smaller bulk Richardson number (Fig. 1d). Vertical exchange between layers thereby became feasible. Accordingly, nighttime concentrations of CO_2 and CH_4 remained at relatively low values (Fig. 1e), and $PM_{2.5}$ also stayed at a low background level (Fig. 1f). The diurnal peak of $PM_{2.5}$ concentrations occurred at 09:00–10:00, with a slight delay relative to the morning rush hour owing to advection from upstream areas. The concentration variations in Stage 1 and Stage 2 clearly demonstrate that, distinct from regionally transported $PM_{2.5}$, the variations in CO_2 and CH_4 from local sources and sinks are significantly influenced by boundary-layer processes (e.g., turbulent diffusion).

In Stage 3, the variations in the concentrations of CO_2, CH_4, and $PM_{2.5}$ were further affected by synoptic-scale processes, agricultural activities, and biological rhythms. According to meteorological records, precipitation occurred on 27 August, consistent with the drops in air temperature and net radiation (Fig. 1a), as well as the wind direction shift (Fig. 1b). Precipitation promoted the wet scavenging of $PM_{2.5}$, leading to a concentration decrease of approximately 37 μg m^{-3} (Fig. 1f). Ramp structures were observed on both sides of this concentration drop. Considering its timescale of 4–5 days, the gradual increases in $PM_{2.5}$ concentration are inferred to be linked to continuous transport driven by synoptic circulations. A substantial increase in CO_2 concentration initially appeared on 22 August, following a shift to southeasterly winds (Fig. 1b). It has been indicated that southeasterly winds could transport anthropogenic CO_2 from the Yangtze River Delta to the paddy fields (Yang et al., 2025). In addition, rice entered the ripening stage at this time, with leaves senescing and yellowing. Weakened photosynthesis reduced the vegetation uptake of CO_2, leading to an overall increase in CO_2 concentration (Fig. 1e). Furthermore, the depletion of field irrigation suppressed the activity of methanogens and simultaneously enhanced the oxidation capacity of methanotrophs, leading to a decrease in CH_4 concentrations to approximately 3.1 ppm.

https://doi.org/10.5194/egusphere-2026-3201
Preprint. Discussion started: 1 September 2026
© Author(s) 2026. CC BY 4.0 License.

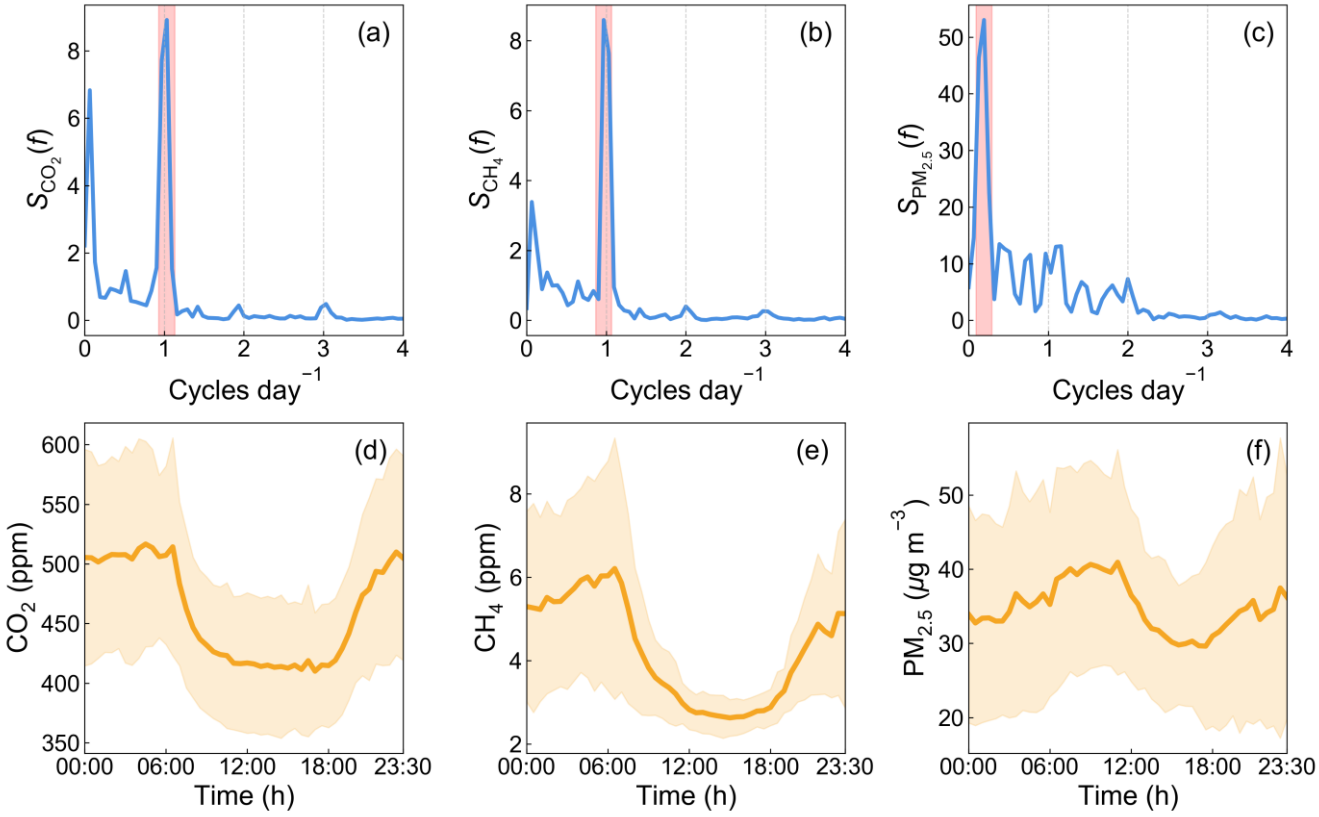

Figure 2. (a–c) Power spectral density and (d–f) diurnal variations of (a, d) CO_2, (b, e) CH_4, and (c, f) $PM_{2.5}$ concentrations at the Shouxian paddy site in August 2024. The red shaded areas highlight the dominant frequencies of each concentration spectrum in (a–c). Yellow lines and the shaded areas represent the average concentrations and associated error range ($\pm\sigma$) over the entire observation period.

To elucidate the multi-scale evolution of CO_2, CH_4, and $PM_{2.5}$ concentrations during the observation period, Fig. 2 presents their power spectral density and average diurnal variations. Distinct dominant peaks appear at the diurnal scale (one cycle per day) for both CO_2 and CH_4 spectra (Figs. 2a–b). In contrast, the peak of $PM_{2.5}$ spectrum occurs at a lower frequency, corresponding to a 5-day cycle, along with a weaker diurnal peak (Fig. 2c). The results agree well with those in Fig. 1, further suggesting that over paddy fields CO_2 and CH_4 concentrations are primarily controlled by boundary-layer processes. Without local sources/sinks, $PM_{2.5}$ concentrations are dominated by advective transport, and show weaker dependence on boundary-layer evolution. On the diurnal scale, both CO_2 and CH_4 concentrations exhibit a pattern of higher at night and lower during the daytime (Figs. 2d–e). Notably, CH_4 production becomes more active at night in the late rice growth stage, leading to an obvious accumulation of CH_4 before sunrise (roughly 06:30). On the other hand, the diurnal peak of $PM_{2.5}$ concentration occurs at approximately 10:00 (Fig. 2f), slightly lagging behind the morning rush hour. This lag is likely attributable to the advection

https://doi.org/10.5194/egusphere-2026-3201
Preprint. Discussion started: 1 September 2026
© Author(s) 2026. CC BY 4.0 License.

of $PM_{2.5}$ emitted from upwind regions. In addition, the wider error range in the average diurnal cycle of $PM_{2.5}$ also reflects its substantial day-to-day variability.

To quantify the role of turbulent transport, Fig. 3 shows the mean diurnal variations of TKE, momentum flux, sensible heat flux, latent heat flux, CO_2 flux, and CH_4 flux during the observation period. Generally, all these turbulent statistics exhibit a distinct unimodal pattern. During the daytime, driven jointly by positive buoyancy and stronger winds (Fig. 1b), the value of TKE is larger, peaking at 0.56 $m^2 s^{-2}$ around 14:00 (Fig. 3a). Vigorous turbulence facilitates the vertical transport of energy and substance efficiently, and thus turbulent fluxes reach their maximum absolute values around noon. At night, turbulent activity weakens and TKE remains at a low level, resulting in suppressed turbulent transport. Owing to frictional effects over the rough underlying surface, momentum is transported downward throughout the day, suggested by negative momentum fluxes (Fig. 3b). Over the paddy fields, latent heat flux is considerably greater than sensible heat flux, with peak values approximately 400 W m^{-2} and 40 W m^{-2}, respectively (Figs. 3c–d). This feature well reflects the partitioning of surface available energy over a moist land surface.

Subtropical paddy fields act as a carbon sink, which is clearly evidenced by the prominent downward transport of CO_2 (Fig. 3e). The average CO_2 flux reaches −37.95 μmol $m^{-2} s^{-1}$ during the daytime, approximately three times that of semi-arid sparse grasslands (Zhang et al., 2023) and twice that of croplands in North China (i.e., Sun et al., 2026). At night, CO_2 is released via ecosystem respiration and transported upward though its magnitude is much smaller, which will be demonstrated in detail in Section 4.2. Different from CO_2 flux, CH_4 flux remains positive throughout the day, indicating that the paddy field serves as an efficient CH_4 source. The magnitude of CH_4 flux is also governed by turbulence intensity. Additionally, the daytime CH_4 flux exhibits a plateau of approximately 0.35 μmol $m^{-2} s^{-1}$ rather than a peak, which may be attributed to reduced CH_4 production at noon. Overall, the transport processes induced by vigorous daytime turbulence can be well characterized by turbulent fluxes. In contrast, the small nighttime flux, which possibly contains large uncertainties associated with intermittent turbulence, cannot resolve the underlying physical mechanisms. Accordingly, the occurrence of intermittent turbulence and its influences on substance dispersion will be focused on in the next section.

https://doi.org/10.5194/egusphere-2026-3201
Preprint. Discussion started: 1 September 2026
© Author(s) 2026. CC BY 4.0 License.

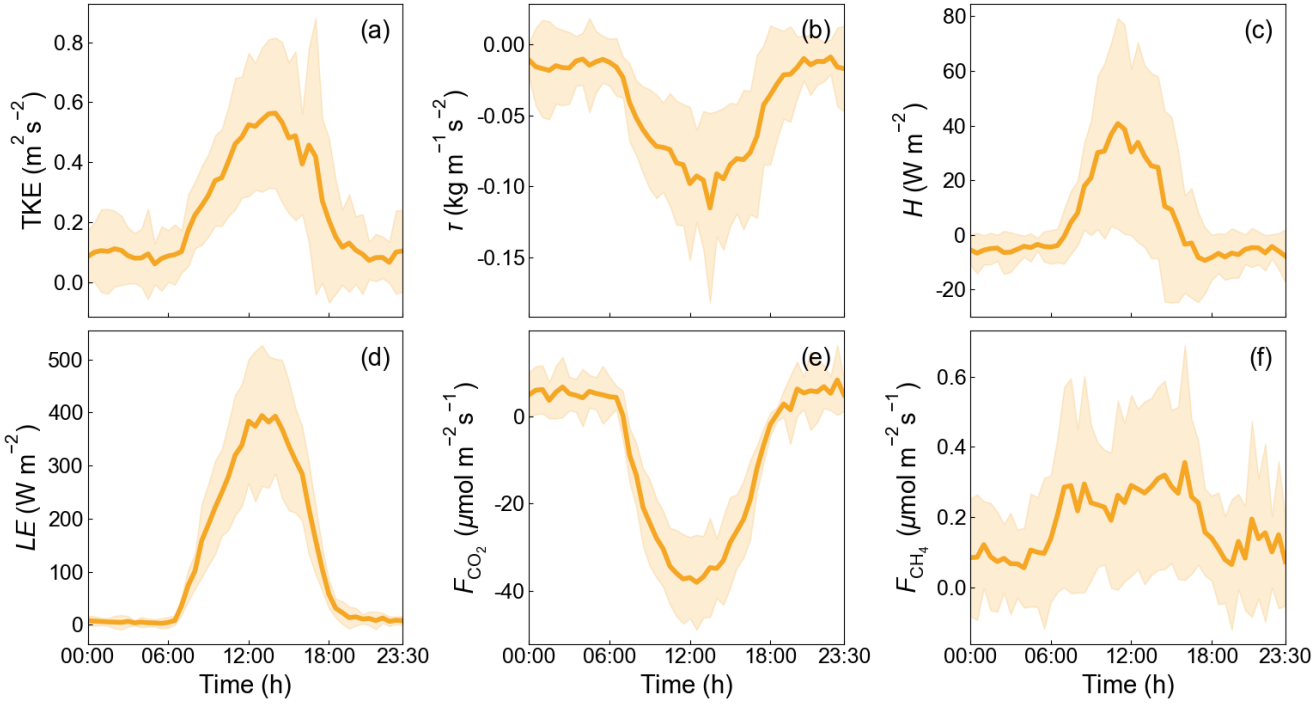

285 **Figure 3. Diurnal variations of (a) turbulent kinetic energy, (b) momentum flux, (c) sensible heat flux, (d) latent heat flux, (e) CO_2 flux, and (f) CH_4 flux at the Shouxian paddy field in August 2024. Yellow lines and shaded areas represent the averaged values and associated error range (±σ) over the entire observation period.**

4.2 Turbulent intermittency and its relations with substance concentrations

290 Figure 4 presents the relationships of both turbulence strength $V_{TKE} = \sqrt{TKE}$ and LIST with wind speed under stable conditions. It can be found that the hockey-stick transition (HOST) model proposed by Sun et al. (2012) also observed over paddy fields (Fig. 4a). Specifically, under low-wind-speed conditions, V_{TKE} increases slowly with increasing wind speed, referred to as weak turbulence regime. In contrast, at high wind speeds, V_{TKE} increases systematically with wind speed, corresponding to the strong turbulence regime. The wind-speed threshold separating these two regimes is 1.5 m s^{-1} over the paddy field (Fig. 4a).
295 In addition, as mentioned in Section 3.1, a LIST threshold of 0.75 is adopted to distinguish intermittent turbulence from continuous turbulence. Notably, wind speeds are generally less than 1.5 m s^{-1} when LIST < 0.75 (Fig. 4b). This correspondence implies that weak turbulence within the HOST framework is closely coupled with intermittent turbulence. Wind speed plays a critical role in determining turbulent states under stable conditions. Actually, wind-speed thresholds vary regionally depending on land-surface characteristics. For instance, Zhang et al. (2024) reported a threshold of 2.5 m s^{-1} over desert
300 surfaces due to enhanced nocturnal surface cooling. Physically, the wind-speed threshold can be understood as the critical value at which turbulence generated by wind shear balances the dissipation caused by negative buoyancy.

https://doi.org/10.5194/egusphere-2026-3201
Preprint. Discussion started: 1 September 2026
© Author(s) 2026. CC BY 4.0 License.

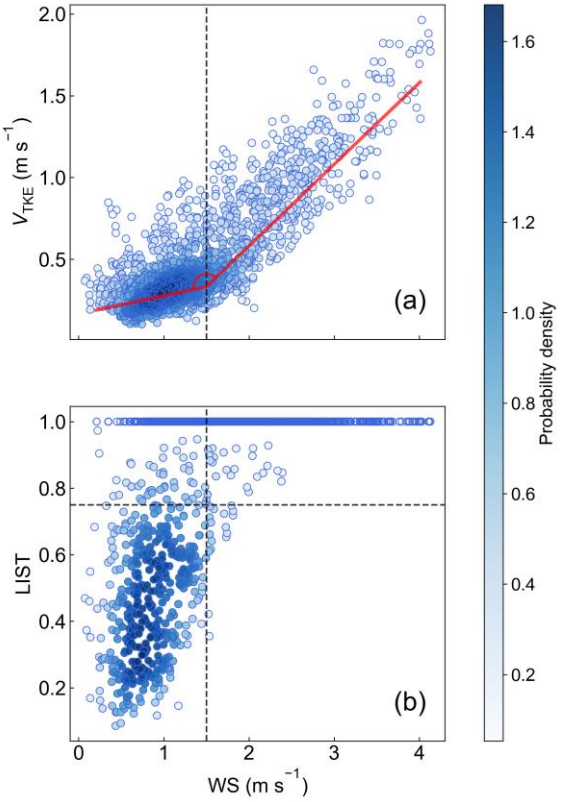

Figure 4. Relationships between (a) $V_{TKE} = \sqrt{TKE}$ and wind speed, as well as (b) LIST and wind speed under stable conditions in August 2024. Darker colour of scatters denotes higher probability density. In panel (a), the black vertical dashed line marks the wind-speed threshold of 1.5 m s^{-1} separating the two regimes highlighted by the thick red line. In panel (b), the black horizontal and vertical dashed lines denote the LIST threshold of 0.75 and the wind-speed threshold of 1.5 m s^{-1}, respectively.

To examine the relation between intermittent turbulence and substance concentrations, Fig. 5 shows the proportions of intermittent and continuous turbulence across different concentration levels under nocturnal stable conditions. Here, intermittent and continuous turbulence are distinguished using the LIST threshold of 0.75. For a given substance, intermittent turbulence accounts for a larger proportion at its higher concentration levels. This result also indicates that weak, intermittent turbulence restricts the vertical dispersion of substances. Moreover, it is notable that CH_4 and CO_2 concentrations are more sensitive to turbulence intermittency than $PM_{2.5}$, suggested by the higher proportion of intermittent turbulence at high concentration levels. This difference is expected because, in addition to intermittent turbulence, high $PM_{2.5}$ concentrations can also be caused by advective transport. The effects of intermittent turbulence on CH_4 and CO_2 concentrations can be further demonstrated using detailed cases in Stage 1. As shown in Fig. 6, LIST values are generally below the threshold during nighttime periods with wind speeds smaller than 1.5 m s^{-1}, indicating intermittent turbulence. Under such conditions, both CO_2 and CH_4 concentrations are high, particularly on the nights of 4 and 5 August. Despite large-amplitude concentration fluctuations (Figs. 6a–6b), efficient vertical transport is inhibited by weak vertical velocity (Fig. 6c). Nevertheless, several

https://doi.org/10.5194/egusphere-2026-3201
Preprint. Discussion started: 1 September 2026
© Author(s) 2026. CC BY 4.0 License.

noteworthy exceptions are observed. For instance, there is a noticeable decrease in both CO_2 and CH_4 concentrations on the night of 4 August (Figs. 6a–b). In the meantime, LIST rises above the threshold (Fig. 6d), indicating a short recovery of turbulence. The transition from quiescent turbulence to short bursts without wind speed exceeding its threshold, is likely attributable to interactions between submeso motions and weak turbulence (e.g., Sun et al., 2015a; b). The breakdown of submeso motions supplies energy for turbulence recovery. Following the short recovery of turbulence, surface CO_2 and CH_4 are rapidly dispersed upward, corresponding to the enhanced fluctuations in both CO_2/CH_4 concentrations and vertical velocity (Figs. 6a–c). This potential physical process is further supported by the drops in CO_2 and CH_4 concentrations, together with elevated LIST (Fig. 6d) at 00:30 and 04:30 on the night of 5 August. Overall, combining the evidence from Figs. 5 and 6, intermittent turbulence generally suppresses the vertical dispersion of CO_2 and CH_4, yet short turbulent bursts can induce their rapid diffusion.

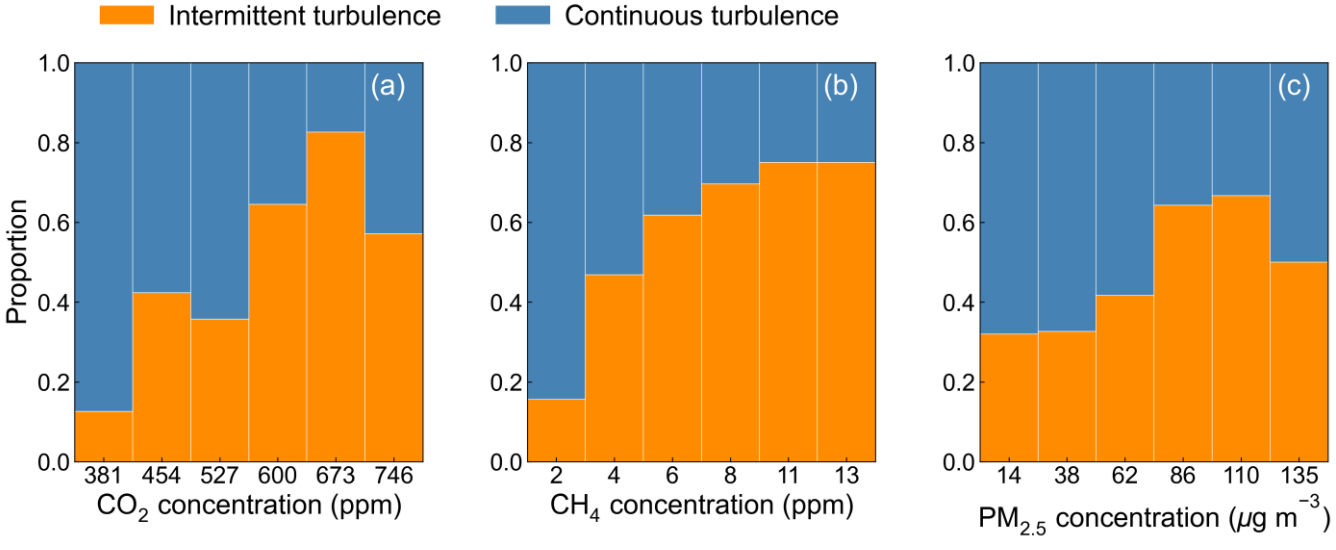

Figure 5. Proportions of intermittent (orange) and continuous (dark blue) turbulence across different concentration levels for (a) CO_2, (b) CH_4, and (c) $PM_{2.5}$ under stable conditions at the Shouxian paddy field in August 2024.

https://doi.org/10.5194/egusphere-2026-3201
Preprint. Discussion started: 1 September 2026
© Author(s) 2026. CC BY 4.0 License.

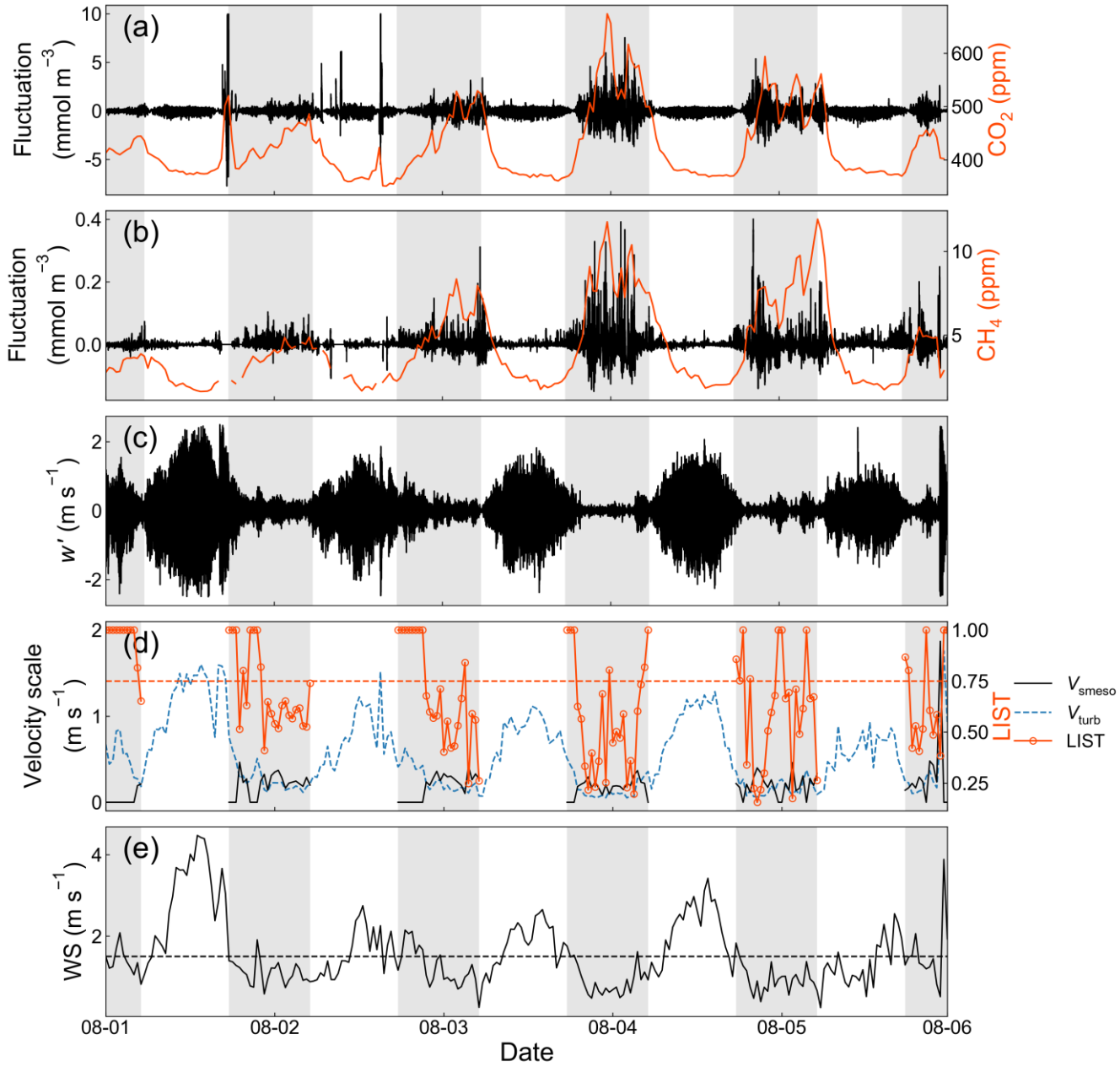

335 **Figure 6. Time series of (a) CO_2 concentration (orange solid line) and its fluctuations (black solid line), (b) CH_4 concentration (orange solid line) and its fluctuations (black solid line), (c) vertical velocity fluctuations, (d) turbulent velocity scale (dark blue dashed lines), submeso velocity scale (black solid line), and LIST (orange solid line with dots), as well as (e) wind speed during the Stage 1. The orange dashed line in panel (d) and black dashed line in panel (e) represent the LIST threshold of 0.75 and the wind-speed threshold of 1.5 m s^{-1}, respectively. The shaded areas represent nighttime.**

340

https://doi.org/10.5194/egusphere-2026-3201
Preprint. Discussion started: 1 September 2026
© Author(s) 2026. CC BY 4.0 License.

Based on mutual information, the occurrence of intermittent turbulence and its effects on substance concentrations are further corroborated. Figure 7 ranks the normalized mutual information between LIST and meteorological variables (e.g., wind speed, air temperature, and specific humidity), as well as the concentrations of CO_2, CH_4, and $PM_{2.5}$. The normalized mutual information between LIST and wind speed is the highest among all variables, which is highly consistent with Fig. 4. That is, mechanical forcing is a key driver of nocturnal turbulence. In contrast, other meteorological variables (i.e., air temperature and specific humidity) exhibit weak nonlinear correlations with LIST, demonstrating their negligible influence on the occurrence of intermittent turbulence. Among the three substances, CH_4 concentration yields the highest mutual information with LIST (with a value of 0.327), followed by CO_2 and $PM_{2.5}$. This ranking agrees well with the results in Fig. 5, implying that CH_4 and CO_2 concentrations are strongly associated with turbulence intermittency under nocturnal stable conditions.

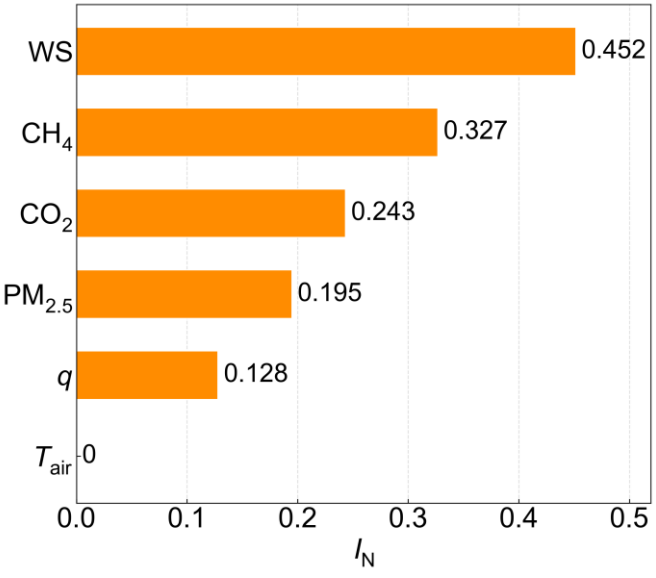

Figure 7. Normalized mutual information between LIST and meteorological variables (wind speed WS, air temperature T_{air}, and specific humidity q), as well as the concentrations of CO_2, CH_4, and $PM_{2.5}$ at the Shouxian paddy field in August 2024.

4.3 Performance of similarity relationships and its improvement

Figure 8 presents the normalized standard deviations of wind components (σ_u/u_* and σ_w/u_*) and potential temperature ($\sigma_\theta/|\theta_*|$) as a function of atmospheric stability parameter ζ. Under near-neutral conditions, σ_u/u_* and σ_w/u_* approach constant values of 2.48 and 1.15, respectively (Figs. 8a–d). These values fairly reflect the underlying surface characteristics of subtropical paddy fields. They are slightly larger than those of grassland due to taller vegetation, much smaller than those within urban canopy layer owing to lower roughness, and comparable to those over flat topography (Table 1). As atmospheric stability/instability increases, both σ_u/u_* and σ_w/u_* gradually increase for continuous turbulence. Their variations with $|\zeta|$ well follow the expected +1/3 power law, as shown by the black dashed lines in Figs. 8a–d. The corresponding fitting functions

https://doi.org/10.5194/egusphere-2026-3201
Preprint. Discussion started: 1 September 2026
© Author(s) 2026. CC BY 4.0 License.

are proposed as follows: $\sigma_u/u_* = 2.48(1-0.07\zeta)^{1/3}$ and $\sigma_w/u_* = 1.15(1-0.04\zeta)^{1/3}$ for unstable conditions, and $\sigma_u/u_* = 2.48(1+0.04\zeta)^{1/3}$ and $\sigma_w/u_* = 1.15(1+0.02\zeta)^{1/3}$ for stable conditions, respectively. However, for intermittent turbulence, σ_u/u_* shows much higher and more scattered values (red circles in Fig. 8b), which considerately deviate from the aforementioned fitting functions. This discrepancy explicitly demonstrates the breakdown of similarity relationships under the prevalence of submeso motions. Furthermore, σ_w/u_* values for intermittent turbulence are lower than those predicted by similarity theory. This is mainly because submeso motions are quasi-horizontal (Mahrt, 2014; Zhang et al., 2024). They generally enhance horizontal velocity fluctuations (and thus increase u_*) while exerting little influence on vertical velocity fluctuations, resulting in reduced σ_w/u_*. After removing submeso components from the originally observed signals (Section 3.1), σ_u/u_* and σ_w/u_* for the reconstructed turbulence fall back within the range described by similarity relationships (orange circles in Figs. 8b and 8d).

https://doi.org/10.5194/egusphere-2026-3201
Preprint. Discussion started: 1 September 2026
© Author(s) 2026. CC BY 4.0 License.

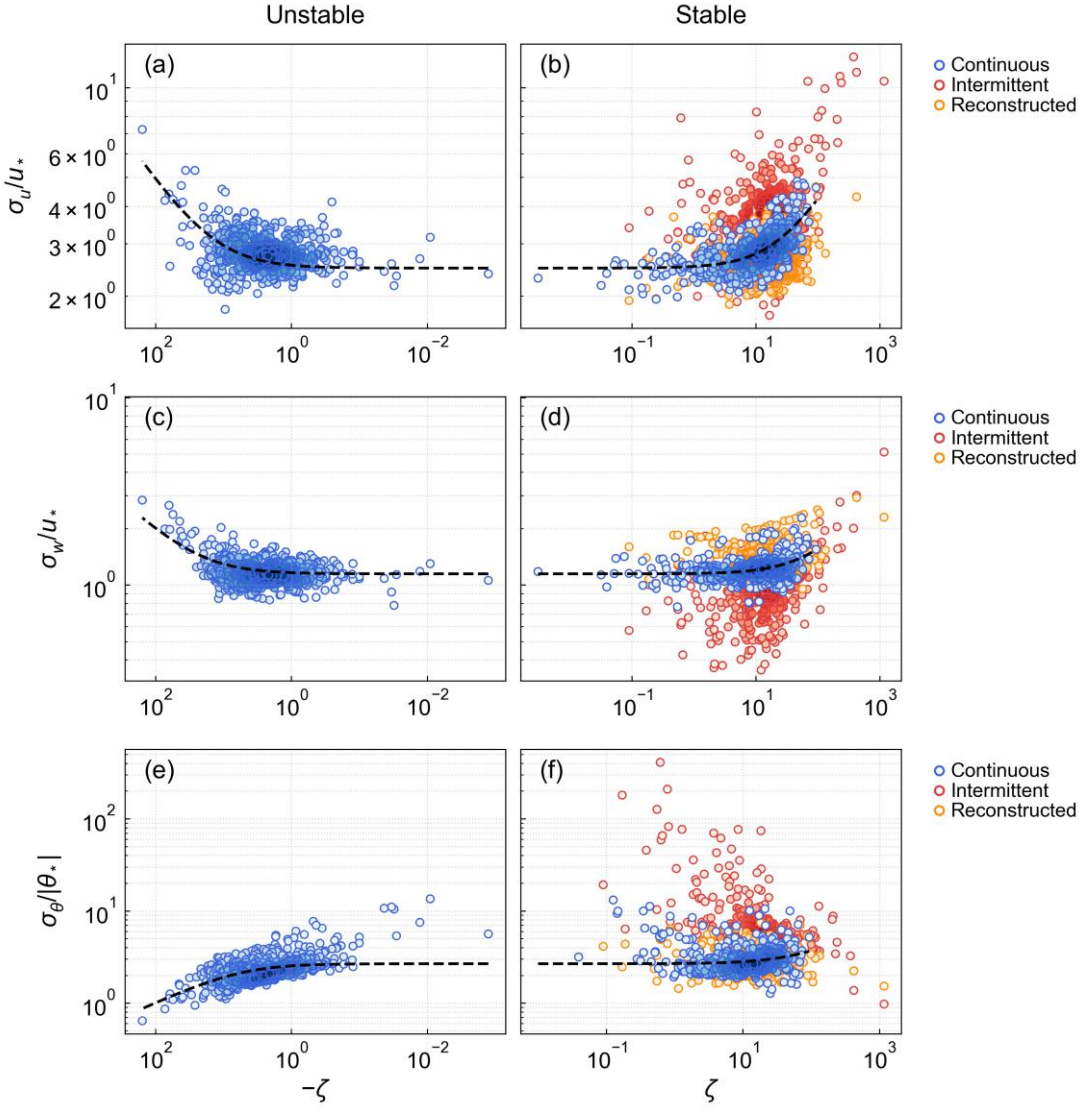

Figure 8. Normalized standard deviations of (a, b) along-wind velocity component σ_u/u_*, (c, d) vertical velocity component σ_w/u_*, and (e, f) potential temperature, $\sigma_\theta/|\theta_*|$ as a function of atmospheric stability parameter ζ. Blue, red, and orange circles denote the samples of continuous, intermittent, and reconstructed turbulence, respectively. Only continuous turbulence is considered here under unstable conditions for comparison. Black dashed lines represent the fitting functions proposed for continuous turbulence, whose mathematical expressions are provided in the text.

Table 1. Normalized standard deviations of wind components under near-neutral conditions over different surface types.

Site	Case Study	σ_u/u_*	σ_w/u_*
Flat topography	Panofsky and Dutton (1984)	2.45	1.25
Grassland	Zhang et al. (2001)	2.29	1.18

https://doi.org/10.5194/egusphere-2026-3201
Preprint. Discussion started: 1 September 2026
© Author(s) 2026. CC BY 4.0 License.

Urban canopy layer	Ren et al. (2018)	3.35	1.57
Gobi Desert	Zhang et al. (2001)	2.62	1.22
Paddy field	This study	2.48	1.15

For $\sigma_\theta/|\theta_*|$, the values decrease with increasing $|\zeta|$ under unstable conditions (Fig. 8e), closely following −1/3 power law. Multiple functional forms have been proposed in previous studies depending on underlying-surface conditions, such as $a(-\zeta)^{-1/3}$ (Hicks, 1981) and $a(1-b\zeta)^{-1/3}$ (De Bruin et al., 1993). In this study, the latter form was adopted based on optimal fitting performance, yielding $\sigma_\theta/|\theta_*| = 2.67(1-0.17\zeta)^{-1/3}$ for unstable conditions. Under stable conditions, $\sigma_\theta/|\theta_*|$ shows a weak increase with the increase of ζ, and the fitting function $2.67(1+0.02\zeta)^{1/3}$ is proposed for continuous turbulence. Notably, the observed $\sigma_\theta/|\theta_*|$ values are higher than the aforementioned fitting curves under near-neutral conditions (Figs. 8e and 8f) because θ_* approaches zero under near-neutral conditions. Furthermore, deviations from similarity theory for intermittent turbulence and the recovery for reconstructed turbulence are confirmed for $\sigma_\theta/|\theta_*|$ under stable conditions (Fig. 8f). Fig. 9 shows the normalized standard deviations of water vapor (σ_q/q_*), CO_2 (σ_{CO_2}/CO_{2*}), and CH_4 (σ_{CH_4}/CH_{4*}) as a function of ζ. Only samples of continuous turbulence are displayed here, given that intermittent and reconstructed turbulence exhibit similar behaviours to those shown in Fig. 8. Overall, σ_q/q_*, σ_{CO_2}/CO_{2*}, and σ_{CH_4}/CH_{4*} vary with ζ in a manner analogous to $\sigma_\theta/|\theta_*|$, with identical functional forms. Specifically, these passive scalars follow the −1/3 power law under unstable conditions and the +1/3 power law under stable conditions. The corresponding fitting functions are expressed as:

$$\frac{\sigma_\theta}{|\theta_*|} = \begin{cases} 2.67(1-0.17\zeta)^{-1/3}, & \zeta < 0 \\ 2.67(1+0.02\zeta)^{1/3}, & \zeta > 0 \end{cases} \quad (24)$$

$$\frac{\sigma_q}{|q_*|} = \begin{cases} 2.22(1-0.03\zeta)^{-1/3}, & \zeta < 0 \\ 2.22(1+0.10\zeta)^{1/3}, & \zeta > 0 \end{cases} \quad (25)$$

$$\frac{\sigma_{CO_2}}{|CO_{2*}|} = \begin{cases} 2.95(1-0.56\zeta)^{-1/3}, & \zeta < 0 \\ 2.95(1+0.02\zeta)^{1/3}, & \zeta > 0 \end{cases} \quad (26)$$

$$\frac{\sigma_{CH_4}}{|CH_{4*}|} = \begin{cases} 8.71(1-0.48\zeta)^{-1/3}, & \zeta < 0 \\ 8.71(1+0.01\zeta)^{1/3}, & \zeta > 0 \end{cases} \quad (27)$$

https://doi.org/10.5194/egusphere-2026-3201
Preprint. Discussion started: 1 September 2026
© Author(s) 2026. CC BY 4.0 License.

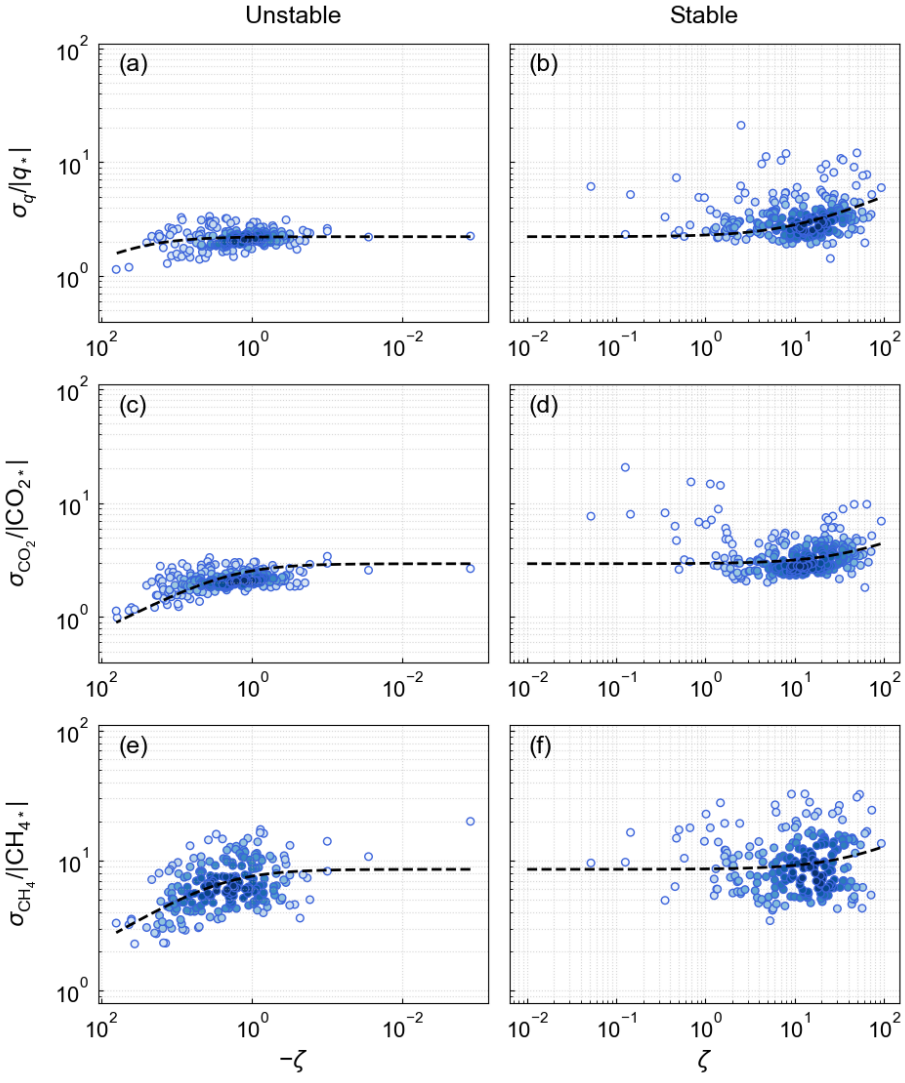

Figure 9. Normalized standard deviations of (a, b) water vapor concentration $\sigma_q/|q_*|$, (c, d) CO_2 concentration $\sigma_{CO_2}/|CO_{2*}|$, and (e, f) CH_4 concentration $\sigma_{CH_4}/|CH_{4*}|$ as a function of atmospheric stability parameter ζ. Only samples from continuous turbulence are presented here. Black dashed lines represent the fitting functions, with their mathematical expressions are provided in the text.

From the perspective of Kolmogorov similarity, Fig. 10 compares energy spectra of u, θ, CO_2, and CH_4 between continuous and intermittent turbulence under stable conditions. The spectra of continuous turbulence under unstable conditions are also shown for reference. In the inertial subrange, the spectra of continuous turbulence closely follow the −2/3 power law. Both u spectra and θ spectra show that, the spectral values of continuous turbulence under stable conditions are slightly higher in the inertial subrange but distinctly lower in the mid-frequency range compared with those under unstable conditions (Figs. 10a and 10b). Meanwhile, spectral peaks shift toward higher frequencies under stable conditions. These characteristics well reflect

https://doi.org/10.5194/egusphere-2026-3201
Preprint. Discussion started: 1 September 2026
© Author(s) 2026. CC BY 4.0 License.

the generally smaller turbulent scales under nocturnal stable conditions. In the energy-containing range, spectral values gradually drop as frequency decreases under unstable conditions, while they tend to flatten out at low frequencies for continuous turbulence under stable conditions. Notably, the spectra for intermittent turbulence under stable conditions exhibit pronounced increases within the low-frequency range and further suppressed magnitudes within a narrowed inertial subrange. They correspond to dominant submeso motions and weakened turbulence, respectively. An energy gap exists between the two regimes. The low-frequency end of the gap represents the minimum scale affected by submeso motions, defined as the critical frequency (Zhang et al., 2024). Over the paddy field, the normalized critical frequency is approximately 0.03. With an observational height of 4 m, the minimum horizontal scale of submeso motions (i.e., $\bar{U}/f$) is roughly 133 m. Such spectral signatures are also observed in spectra of CO_2 and CH_4 (Figs. 10c and 10d), further demonstrating that submeso motions exert considerable impacts on their concentration variations during turbulent intermittency, consistent with the results in Fig. 9.

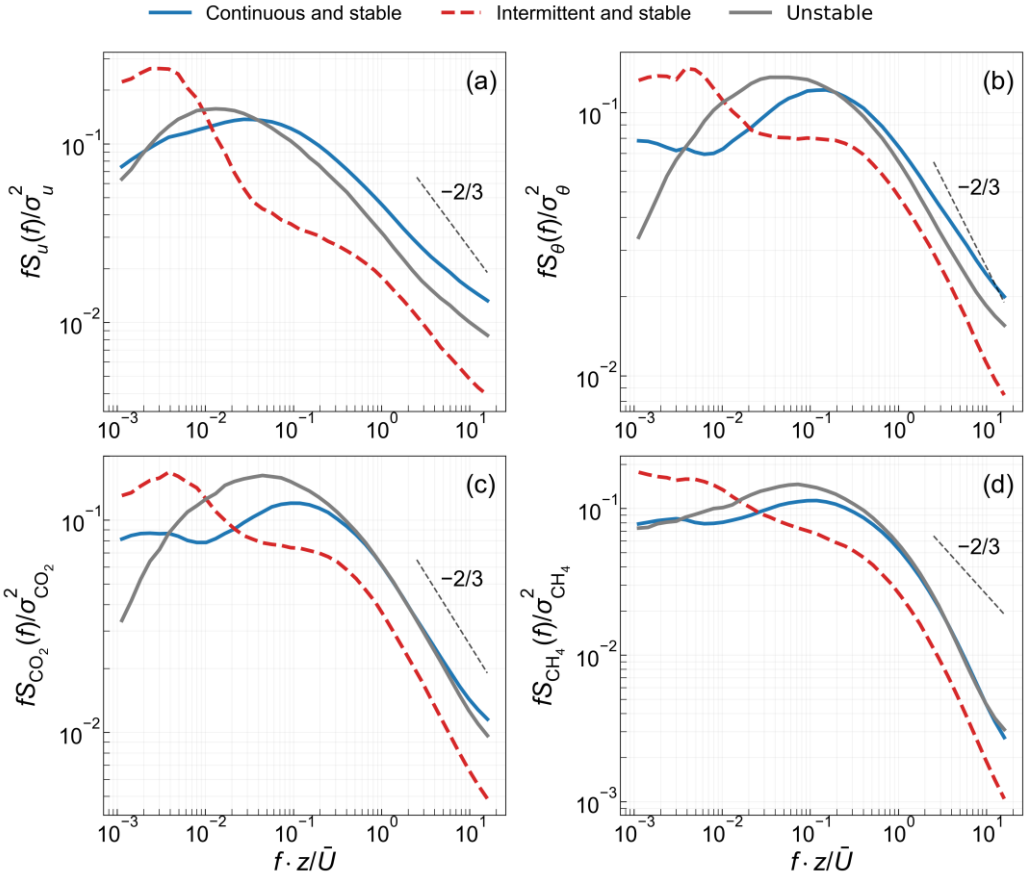

Figure 10. Normalized energy spectra of (a) along-wind velocity component, (b) potential temperature, (c) CO_2 concentration, and (d) CH_4 concentration. Blue solid, red dashed, and grey solid lines denote continuous turbulence under stable conditions, intermittent turbulence under stable conditions, and continuous turbulence under unstable conditions, respectively. The reference slope of −2/3 is plotted by black dashed lines. All energy spectra are normalized by variances, and the natural frequency is normalized using the horizontal wind speed and observation height.

https://doi.org/10.5194/egusphere-2026-3201
Preprint. Discussion started: 1 September 2026
© Author(s) 2026. CC BY 4.0 License.

The appearance of spectral gap for intermittent turbulence in Fig. 10 suggests a disruption of energy cascade. To further support this, Fig. 11 presents the variation of incremental self-mutual information of fluctuations with time lag under stable conditions. The time lag τ is normalized by the integral time scale τ_0 which characterizes the lifetime of dominant turbulent eddies. For all four fluctuation quantities, mutual information is generally smaller at short time lags. This demonstrates that small-scale eddies dissipate rapidly, and thus a limited amount of information (i.e., related to energy) is retained. Additionally, intermittent turbulence consistently exhibits higher incremental self-mutual information than continuous turbulence for a given time lag. The feature becomes more pronounced when $\tau/\tau_0 > 1$, particularly for scalar fluctuations (Figs. 11b–11d). Physically, this discrepancy arises from the breakdown of energy cascade for intermittent turbulence (Mahrt, 2014). The information carried by large-scale motions, such as energy carried by submeso motions, is trapped within its original scale, thereby increasing the mutual information values. Moreover, the incremental self-mutual information of along-wind velocity fluctuations (Fig. 11a) is obviously lower than that of other three scalars (Figs. 11b–11d). This result implies a lower predictability of horizontal turbulent velocity, primarily due to the direct influence of submeso motions on horizontal flow fluctuations.

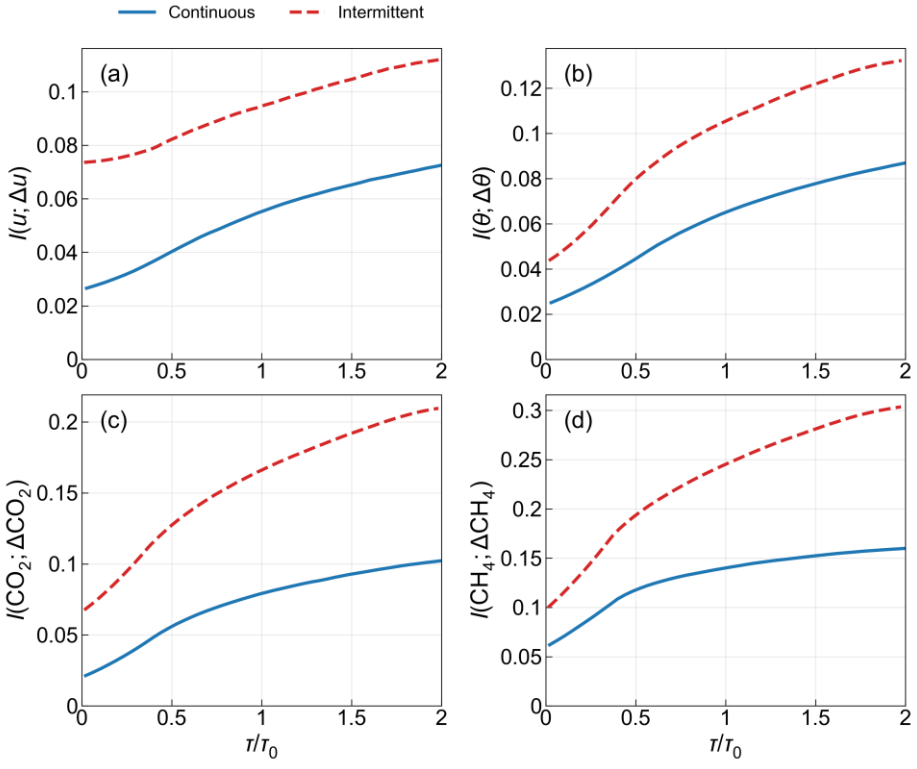

Figure 11. Incremental self-mutual information of (a) along-wind velocity fluctuations, (b) potential temperature fluctuations, (c) CO_2 concentration fluctuations, and (d) CH_4 concentration fluctuations as a function of time lag normalized by the integral time scale under stable conditions. Blue solid and red dashed lines denote continuous and intermittent turbulence, respectively. Note that the vertical axis ranges differ among panels.

https://doi.org/10.5194/egusphere-2026-3201
Preprint. Discussion started: 1 September 2026
© Author(s) 2026. CC BY 4.0 License.

5. Conclusion

The effects of atmospheric turbulence on the vertical dispersion of CO_2 and CH_4 were investigated using high-frequency observations over subtropical paddy fields. Paddy fields are typical sources of CH_4 and sinks of CO_2 (while acting as CO_2 sources at night), consistent with the directions of their turbulent fluxes. Both surface CO_2 and CH_4 concentrations exhibit significant diurnal cycles, indicating that they are strongly influenced by boundary-layer processes (i.e., turbulent diffusion), in addition to the biological activity of rice plants. Special attention was given to nocturnal stable conditions, and mutual information was introduced to characterize the relevant nonlinear processes. When wind speed is lower than 1.5 m s^{-1}, turbulence becomes intermittent. Under such conditions, both CO_2 and CH_4 accumulate near the surface, resulting in elevated concentrations. Once turbulence temporarily recovers (i.e., during short bursts), surface CO_2 and CH_4 are rapidly dispersed upward, and their concentrations decrease sharply. Mutual information analysis further supports that the occurrence of intermittent turbulence is strongly controlled by wind speed and exerts a significant influence on CO_2 and CH_4 concentrations. Under intermittent turbulence, classic similarity relationships become invalid for characterizing the transport of momentum, heat, as well as the passive scalars CO_2 and CH_4. This inconsistency is primarily caused by the interference of submeso motions. After removing submeso components from the original observational signals, the reconstructed turbulence conforms to the framework of similarity theory. Furthermore, the distinct spectral gap between submeso and turbulent scales provides evidence for the breakdown of energy cascade. Specifically, the information (e.g., energy) associated with submeso motions remains confined to its original scales, which limits the energy supply for small-scale turbulence and renders turbulent motions more stochastic. This study reveals that the vertical dispersion of CO_2 and CH_4 over paddy fields is substantially modulated by intermittent turbulence under nocturnal stable conditions, and highlights that the considerable challenges remain in accurately parameterizing such boundary-layer transport processes. These findings provide new insights into improving the quantitative evaluation of terrestrial carbon cycling and greenhouse-gas budgets.

Code/Data availability

Code/Data used in this study are available from the corresponding author upon request (luzhang@nuist.edu.cn).

Author contributions

JY and LZ completed the initial data analysis, and wrote the main manuscript. JY and YX plotted the all figures. XL and WD collected the experimental data. Further discussions were done by YL and YW. LZ and YY conceptualized the study. All authors reviewed and revised the manuscript.

https://doi.org/10.5194/egusphere-2026-3201
Preprint. Discussion started: 1 September 2026
© Author(s) 2026. CC BY 4.0 License.

Competing interests

The contact author has declared that none of the authors has any competing interests.

Acknowledgment

This work is funded by the National Natural Science Foundation of China (Nos. 42521006 and 42505082) and the Natural Science Foundation of Jiangsu Province, China (No. BK20250750). The authors gratefully acknowledge the Shouxian National Climatology Observatory for providing the observational data used in this study.

References

Acevedo, O. C., Costa, F. D., Oliveira, P. E. S., Puhales, F. S., Degrazia, G. A., and Roberti, D. R.: The influence of submeso processes on stable boundary layer similarity relationships, J. Atmos. Sci., 71, 207–225, https://doi.org/10.1175/JAS-D-13-0131.1, 2014.

Bahamonde, A. D., Cornejo, P., and Sepúlveda, H. H.: Laminar to turbulent transition in terms of information theory, Physica A, 629, 129190, https://doi.org/10.1016/j.physa.2023.129190, 2023.

Businger, J. A., Wyngaard, J. C., Izumi, Y., and Bradley, E. F.: Flux-profile relationships in the atmospheric surface layer, J. Atmos. Sci., 28, 181–189, https://doi.org/10.1175/1520-0469(1971)028<0181:FPRITA>2.0.CO;2, 1971.

Cover, T. M., and Thomas, J. A.: Elements of Information Theory, John Wiley & Sons, New York, https://doi.org/10.1002/047174882X, 2006.

De Bruin, H. A. R., Kohsiek, W., and Van den Hurk, B.: A verification of some methods to determine the fluxes of momentum, sensible heat, and water-vapor using standard-deviation and structure parameter of scalar meteorological quantities, Bound.-Layer Meteorol., 63, 231–257, https://doi.org/10.1007/BF00710461, 1993.

Detto, M., Katul, G., Mancini, M., Albertson J. D.: Surface heterogeneity and its signature in higher-order scalar similarity relationships, Agric. For. Meteorol., 148, 902–916, https://doi.org/10.1016/j.agrformet.2007.12.008, 2008.

Duan, Z. X., Gao, Z. Q., Xu, Q., Zhou, S. H., Qin, K., and Yang, Y. J.: A benchmark dataset of diurnal- and seasonal-scale radiation, heat, and CO_2 fluxes in a typical East Asian monsoon region, Earth Syst. Sci. Data, 14, 4153–4169, https://doi.org/10.5194/essd-14-4153-2022, 2022.

Foken, T.: Micrometeorology, Springer-Verlag, Berlin Heidelberg, https://doi.org/10.1007/978-3-540-74666-9, 2008.

Grachev, A. A., Fairall, C. W., Persson, P. O. G., Andreas, E. L., and Guest, P. S.: Stable boundary-layer scaling regimes: the SHEBA data, Bound.-Layer Meteorol., 116, 201–235, https://doi.org/10.1007/s10546-004-2729-0, 2005.

Hicks, B. B.: An examination of turbulence statistics in the surface boundary layer, Bound.-Layer Meteor., 21, 389-402, 10.1007/BF00119379, 1981.

https://doi.org/10.5194/egusphere-2026-3201
Preprint. Discussion started: 1 September 2026
© Author(s) 2026. CC BY 4.0 License.

Huang, Y. X., Schmitt, F. G., Lu, Z. M., and Liu, Y. L.: An amplitude-frequency study of turbulent scaling intermittency using empirical mode decomposition and Hilbert spectral analysis, Europhys. Lett., 84, 40010, https://doi.org/10.1209/0295-5075/84/40010, 2008.

Ikeda, K., and Matsumoto, K.: Information theoretical characterization of turbulence, Phys. Rev. Lett., 62, 2265–2268, https://doi.org/10.1103/PhysRevLett.62.2265, 1989.

IPCC: Climate Change 2021–The Physical Science Basis, Contribution of Working Group I to the Sixth Assessment Report, Cambridge University Press, 2391 pp., https://doi.org/10.1017/9781009157896, 2021.

Jason A. Otkin, Lee M. Cronce, Jonathan L. Case, R. Bradley Pierce, Monica Harkey, Allen Lenzen, David S. Henderson, Zac Adelman, Tsengel Nergui, and Christopher R. Hain: Meteorological modeling sensitivity to parameterizations and satellite-derived surface datasets during the 2017 Lake Michigan Ozone Study, Atmos. Chem. Phys., 23, 7935–7954, https://doi.org/10.5194/acp-23-7935-2023, 2023.

Jiménez, P. A., Dudhia, J., González-Rouco, J. F., Navarro, J., Montávez, J. P., and García-Bustamante, E.: A revised scheme for the WRF surface layer: Formulation and evaluation, Mon. Weather Rev., 140, 898–918, https://doi.org/10.1175/MWR-D-11-00056.1, 2012.

Kaimal, J. C., Wyngaard, J. C., Izumi, Y., and Coté, O. R.: Spectral characteristics of surface-layer turbulence, Q. J. Roy. Meteorol. Soc., 98, 563–589, https://doi.org/10.1002/qj.49709841707, 1972.

Mahrt, L.: Characteristics of submeso winds in the stable boundary layer, Bound.-Layer Meteorol., 130, 1–14, https://doi.org/10.1007/s10546-008-9336-4, 2009.

Mahrt, L.: Stably stratified atmospheric boundary layers, Annu. Rev. Fluid Mech., 46, 23–45, https://doi.org/10.1146/annurev-fluid-010313-141354, 2014.

McGill, W. J.: Multivariate Information Transmission, Psychometrika, 19, 97–116, https://doi.org/10.1007/BF02289159, 1954.

Monin, A. S., and Obukhov, A. M.: Basic turbulent mixing laws in the atmospheric boundary layer, Trudy Geofiz. Inst. AN SSSR, 24, 163–187, 1954.

MEE (Ministry of Ecology and Environment): The People's Republic of China Fourth Biennial Update Report on Climate Change, Ministry of Ecology and Environment of the People's Republic of China, Beijing, China, 66 pp., available at: https://unfccc.int/sites/default/files/resource/The People's Republic of China Fourth Biennial Update Report on Climate Change.pdf, 2024.

Mohammad Allouche, Vladislav I. Sevostianov, Einara Zahn, Mark A. Zondlo, Nelson Luís Dias, Gabriel G. Katul, Jose D. Fuentes, and Elie Bou-Zeid: Estimating scalar turbulent fluxes with slow-response sensors in the stable atmospheric boundary layer, Atmos. Chem. Phys., 24, 9697–9711, https://doi.org/10.5194/acp-24-9697-2024, 2024.

Nappo, C. J., Sun, J., Mahrt, L., and Belušić, D.: Determining Wave–Turbulence Interactions in the Stable Boundary Layer, Bull. Amer. Meteorol. Soc., 95, ES11–ES13, https://doi.org/10.1175/BAMS-D-12-00235.1, 2014.

Panofsky, H. A. and Dutton, J. A.: Atmospheric Turbulence: Models and Methods for Engineering Applications, Wiley, New York, ISBN 9780471057147, 1984.

https://doi.org/10.5194/egusphere-2026-3201
Preprint. Discussion started: 1 September 2026
© Author(s) 2026. CC BY 4.0 License.

Raj, R., Thiruthummal, A., and Pothérat, A.: Detecting turbulent patterns in particulate pipe flow by streak–angle visualization, Exp. Fluids, 66, 144, https://doi.org/10.1007/s00348-025-04065-2, 2025.

Ren, Y., Zheng, S. W., Wei, W., Wu, B. G., Zhang, H. S., Cai, X. H., and Song, Y.: Characteristics of turbulent transfer during episodes of heavy haze pollution in Beijing in winter 2016/17, J. Meteorol. Res., 32, 69–80, https://doi.org/10.1007/s13351-018-7072-3, 2018.

Ren, Y., Zhang, H. S., Wei, W., Wu, B. G., Cai, X. H., and Song, Y.: Effects of turbulence structure and urbanization on the heavy haze pollution process, Atmos. Chem. Phys., 19, 1041–1057, https://doi.org/10.5194/acp-19-1041-2019, 2019.

Ren, Y., Zhang, H. S., Zhang, X. Y., Wei, W., Li, Q., Wu, B. G., Cai, X. H., Song, Y., Kang, L., and Zhu, T.: Turbulence barrier effect during heavy haze pollution events, Sci. Total Environ., 753, 142286, https://doi.org/10.1016/j.scitotenv.2020.142286, 2021.

Shannon, C. E.: A mathematical theory of communication, ACM SIGMOBILE Mobile Computing and Communications Review, 5, 3–55, https://doi.org/10.1145/584091.584093, 1948.

Shannon, C. E.: Communication in the Presence of Noise, Proceedings of the IRE, 37, 10–21, https://doi.org/10.1109/jrproc.1949.232969, 1949.

Shavit, M. and Falkovich, G.: Singular Measures and Information Capacity of Turbulent Cascades, Phys. Rev. Lett., 125, 104501, https://doi.org/10.1103/PhysRevLett.125.104501, 2020.

Salmond, J. A.: Wavelet analysis of intermittent turbulence in a very stable nocturnal boundary layer: Implications for the vertical mixing of ozone, Bound.-Layer Meteorol., 114, 463–488, https://doi.org/10.1007/s10546-004-2422-3, 2005.

Stull, R. B.: An Introduction to Boundary Layer Meteorology, Kluwer Academic Publishers, Dordrecht, https://doi.org/10.1007/978-94-009-3027-8, 1988.

Sun, J., Mahrt, L., Banta, R. M., and Pichugina, Y. L.: Turbulence regimes and turbulence intermittency in the stable boundary layer during CASES-99, J. Atmos. Sci., 69, 338–351, https://doi.org/10.1175/JAS-D-11-082.1, 2012.

Sun, J., Mahrt, L., Nappo, C., and Lenschow, D. H.: Wind and Temperature Oscillations Generated by Wave–Turbulence Interactions in the Stably Stratified Boundary Layer, J. Atmos. Sci., 72, 1484–1503, https://doi.org/10.1175/JAS-D-14-0129.1, 2015a.

Sun, J., Nappo, C. J., Mahrt, L., Belušić, D., Grisogono, B., Stauffer, D. R., Pulido, M., Staquet, C., Jiang, Q., Pouquet, A., Yagüe, C., Galperin, B., Smith, R. B., Finnigan, J. J., Mayor, S. D., Svensson, G., Grachev, A. A., and Neff, W. D.: Review of wave-turbulence interactions in the stable atmospheric boundary layer, Rev. Geophys., 53, 956-993, 10.1002/2015rg000487, 2015b.

Sun, Q., Zhang, L., Xue, J., Wang, L., Li, Y., and Yang, Y.: Comparison of turbulent transport dissimilarity and the role of coherent structures in the unstable surface layer between urban and rural areas, Bound.-Layer Meteorol., 192, 34, https://doi.org/10.1007/s10546-026-00978-5, 2026.

https://doi.org/10.5194/egusphere-2026-3201
Preprint. Discussion started: 1 September 2026
© Author(s) 2026. CC BY 4.0 License.

Tamanna Subba, Michael P. Jensen, Min Deng, Scott E. Giangrande, Mark C. Harvey, Ashish Singh, Die Wang, Maria Zawadowicz, and Chongai Kuang: Implications of Sea Breeze Circulations on boundary layer aerosols in the southern coastal Texas region, Atmos. Chem. Phys., 26, 2853–2879, https://doi.org/10.5194/acp-26-2853-2026, 2026.

Tang, G., Zhang, J., Zhu, X., Song, T., Münkel, C., Hu, B., Schäfer, K., Liu, Z., Zhang, J., Wang, L., Xin, J., Suppan, P., and Wang, Y.: Mixing layer height and its implications for air pollution over Beijing, China, Atmos. Chem. Phys., 16, 2459–2475, https://doi.org/10.5194/acp-16-2459-2016, 2016.

Tsuji, Y., and Nakamura, I.: Probability density function in the log-law region of low Reynolds number turbulent boundary layer, Phys. Fluids, 11, 647–658, https://doi.org/10.1063/1.869936, 1999.

Vickers, D., and Mahrt, L.: Quality control and flux sampling problems for tower and aircraft data, J. Atmos. Ocean. Technol., 14, 512–526, https://doi.org/10.1175/1520-0426(1997)014<0512:QCAFSP>2.0.CO;2, 1997.

Wang, H., Xue, M., Zhang, X. Y., Liu, H. L., Zhou, C. H., Tan, S. C., Che, H. Z., Chen, B., and Li, T.: Mesoscale modeling study of the interactions between aerosols and PBL meteorology during a haze episode in Jing–Jin–Ji (China) and its nearby surrounding region – Part 1: Aerosol distributions and meteorological features, Atmos. Chem. Phys., 15, 3257–3275, https://doi.org/10.5194/acp-15-3257-2015, 2015.

Webb, E. K., Pearman, G. I., and Leuning, R.: Correction of flux measurements for density effects due to heat and water vapour transfer, Q. J. R. Meteorol. Soc., 106, 85–100, https://doi.org/10.1002/qj.49710644707, 1980.

Wei, W., Schmitt, F. G., Huang, Y. X., and Zhang, H. S.: The analyses of turbulence characteristics in the atmospheric surface layer using arbitrary-order Hilbert spectra, Bound.-Layer Meteorol., 159, 391–406, https://doi.org/10.1007/s10546-015-0122-9, 2016.

Wei, W., Zhang, H. S., Schmitt, F. G., Huang, Y. X., Cai, X. H., Song, Y., Huang, X., and Zhang, H.: Investigation of turbulence behaviour in the stable boundary layer using arbitrary-order Hilbert spectra, Bound.-Layer Meteorol., 163, 311–326, https://doi.org/10.1007/s10546-016-0227-9, 2017.

Wei, W., Zhang, H., Wu, B., Huang, Y., Cai, X., Song, Y., and Li, J.: Intermittent turbulence contributes to vertical dispersion of $PM_{2.5}$ in the North China Plain: cases from Tianjin, Atmos. Chem. Phys., 18, 12953–12967, https://doi.org/10.5194/acp-18-12953-2018, 2018.

Yang, G. Y., Lu, Y. Y., Huo, Y. F., Zhang, H., Duan, C. F., Ling, X. F., Yan, S. W., Wang, M., and Shen, Y. L.: The characteristics of atmospheric CO_2 concentration changes in the agricultural areas of the Huai River basin, Acta Sci. Circumstantiae, 45, 353–364, https://doi.org/10.13671/j.hjkxxb.2025.0009, 2025 (in Chinese).

Yus-Díez, J., Udina, M., Soler, M. R., Lothon, M., Nilsson, E., Bech, J., and Sun, J.: Nocturnal boundary layer turbulence regimes analysis during the BLLAST campaign, Atmos. Chem. Phys., 19, 9495–9514, https://doi.org/10.5194/acp-19-9495-2019, 2019.

Zhang, H. S., Chen, J. Y., and Park, S. U.: Turbulence structure in unstable conditions over various surfaces, Bound.-Layer Meteorol., 100, 243–261, https://doi.org/10.1023/A:1019223316895, 2001.

https://doi.org/10.5194/egusphere-2026-3201
Preprint. Discussion started: 1 September 2026
© Author(s) 2026. CC BY 4.0 License.

Zhang, L., Zhang, H., Li, Q., Cai, X., and Song, Y.: Vertical dispersion mechanism of long-range transported dust in Beijing: Effect of atmospheric turbulence, Atmos. Res., 269, 106033, https://doi.org/10.1016/j.atmosres.2022.106033, 2022.

Zhang, L., Zhang, H., Li, Q., Wu, B., Cai, X., Song, Y., and Zhang, X.: Complexity of carbon dioxide flux in urban areas: A comparison with natural surfaces, Sci. Total Environ., 895, 165115, https://doi.org/10.1016/j.scitotenv.2023.165115, 2023.

Zhang, L., Zhang, H. S., Cai, X. H., Song, Y., and Zhang, X. Y.: Characteristics of turbulence intermittency, fine structure, and flux correction in the Taklimakan Desert, J. Atmos. Sci., 81, 459–475, https://doi.org/10.1175/JAS-D-23-0107.1, 2024.

Zhang, L., Xue, J., Liao, Y., Ling, X., Ding, W., Li, Y., and Yang, Y.: Revisiting turbulent transport dissimilarities and coherent structure transitions: An observation study from subtropical paddy fields, Agric. For. Meteorol., 384, 111158, https://doi.org/10.1016/j.agrformet.2026.111158, 2026.